EISSN: 2528 - 0112

JURNAL VIRTUAL OF MECHANICAL ENGINEERING ARTICLE (V-MAC)

https://ejournal.unibabwi.ac.id/index.php/vmac email: vmac.mesin@gmail.com

Identifying and Quantifying Maritime-Induced Surface Damage on Cessna 172 Seaplane Brake Calipers via SEM and Image Analysis

Rizki Ocsera[1], Dimas Hari Cahyo[2], Ahmad Mubarok[3], Dimas Endrawan[4], Muhamad Khoirul Anam[5].

[1]Akademi Penerbangan Indonesia, Indonesia, rizkyocsera@gmail.com
[2]Akademi Penerbangan Indonesia, Indonesia, dimashari@icpa-banyuwangi.ac.id
[3]Akademi Penerbangan Indonesia, Indonesia, mubarok@icpa-banyuwangi.ac.id
[4]Politeknik Penerbangan Jayapura, Indonesia, dimas.endrawan@gmail.com
[5]Universitas PGRI Banyuwangi, Indonesia, anamkhoirulm@unibabwi.ac.id

Corresponding Author: dimas.endrawan@gmail.com

Abstract: Seaplane brake components are repeatedly exposed to salt-laden moisture, wet–dry cycles, and surface deposits, while also enduring landing impacts, mechanical vibrations, and braking heat. Despite routine periodic maintenance, these combined stresses still trigger micro-scale damage that escapes visual inspection. This study identifies and quantifies surface damage on a dual-piston Cast Aluminum Alloy A356-T6 brake caliper from a Cessna 172 seaplane using scanning electron microscopy (SEM) and digital image analysis. The specimen is a Parker Cleveland caliper (P/N 091-04400, system 30-75, 8.14 × 7.85 × 3.61 inches, 1.95 lbs), examined specifically on the flat surface between the lower piston bore edge and lower guide pin. Secondary electron images at 300×, 500×, 800×, and 1000× (10 kV) were processed through background correction, adaptive segmentation, object measurement, elongated-feature detection, and fractal analysis, alongside operational records from January 2022–July 2026 (3,891.9 flight hours, 3,442 landings, 1,224 water landings). Results show that the segmented damaged surface area fraction within the SEM field of view ranges from 35.60–39.70% (cross-scale mean: 36.78 ± 1.95%). Pit density reaches 4.01×10^{4}–1.33×10^{5} pits/mm², while the mean equivalent diameter decreases from 1.08 µm (300×) to 0.41 µm (1000×). Based on segmented area profiles, object shapes, and fractal contours, the damage morphology matches pitting, deposit-related attack, exfoliation-like damage, and microcracking. This study provides a quantitative early-detection method to evaluate component serviceability and optimize periodic maintenance, which future research can complement with SEM-EDX elemental verification and mass-loss or electrochemical corrosion-rate testing.

Keyword: aircraft corrosion, A356-T6 aluminum, brake caliper, digital image analysis, scanning electron microscopy.

1. INTRODUCTION

The brake caliper is a critical part of an aircraft braking system. Because it is located in the exposed wheel area, the component repeatedly encounters water spray, salt-laden moisture, runway debris, and wet-dry cycles, while simultaneously enduring landing impacts, mechanical vibrations, and intense braking heat. The thermal and mechanical stresses induced

during landing and braking cycles can compromise protective coatings, induce micro-stresses on the component surface, and exacerbate localized vulnerabilities. Exposure is particularly severe on seaplanes because water landings and surface taxiing leave saline moisture and deposits around the wheel and brake assembly, especially when freshwater rinsing is delayed after operation. The Federal Aviation Administration emphasizes that aircraft corrosion control requires early detection, regular inspection, cleaning, drying, and restoration of protective coatings [1]. In maritime environments, relative humidity, temperature, time of wetness, and airborne salt are among the main factors controlling environmental aggressiveness [2]. Consequently, even when routine periodic maintenance is performed, these combined environmental and mechanical stresses can still trigger micro-scale surface damage that escapes standard visual inspection.

In this study, the investigated specimen is a dual-piston Parker Cleveland brake caliper (P/N 091-04400, system 30-75, measuring 8.14 × 7.85 × 3.61 inches and weighing 1.95 lbs) from a Cessna 172 seaplane, manufactured from Cast Aluminum Alloy A356-T6, which is an Al-Si-Mg casting alloy widely valued for its castability, low density, and mechanical performance. Its microstructure contains an aluminum-rich matrix, eutectic silicon, Mg-containing precipitates, and intermetallic particles. In chloride-bearing environments, electrochemical differences between these phases create local cathodic and anodic sites, weaken the passive film, and promote pit initiation [10], [11].

When subjected to demanding aircraft operational cycles, the interaction between localized corrosion and cyclic mechanical loads introduces severe corrosion-fatigue interactions. This vulnerability is particularly pronounced on the flat caliper body surface located between the lower piston bore edge and the lower guide pin, where saline deposits easily accumulate alongside mechanical and thermal stresses. Pits formed by localized attack act as critical stress concentrators, which, when combined with braking heat and landing vibrations, significantly accelerate crack initiation and propagation. Studies on aircraft-grade and cast aluminum alloys have shown that tropical-maritime exposure accelerates pitting, intergranular attack, and surface-layer separation through the combined action of chloride ions, high humidity, rainfall, and wet-dry cycling [4]-[7]. Sodium chloride deposits on a moist surface form a thin electrolyte film and concentrate attack at specific sites [8]. Pit number, pit size, cracking, and delamination are also influenced by microstructure, porosity, surface condition, coating integrity, and exposure duration [9]-[13].

Scanning electron microscopy (SEM) reveals surface morphology and topography at the micrometer scale. However, visual interpretation of a single image often remains qualitative, relying on descriptions such as rough surfaces or numerous cavities. Digital image analysis makes the assessment measurable by quantifying the segmented damaged surface area fraction within the SEM field of view, object count, pit density, equivalent diameter, elongated-feature length, and fractal contour complexity. This approach aligns with ASTM G46, which emphasizes pit size, number, and distribution in evaluating pitting corrosion [3], and with recent image-processing workflows for corrosion detection [14].

ImageJ was selected because its processing steps, including background correction, adaptive segmentation, object measurement, elongated-feature detection, and fractal analysis, can be documented, repeated, and independently verified [15]-[17]. Based on these 2D geometric parameters, specifically segmented area profiles, object shapes, and fractal contours, surface morphologies corresponding to pitting, deposit-related attack, exfoliation-like damage, and microcracking can be systematically identified. Nevertheless, because SEM image brightness is also influenced by surface geometry, specimen orientation, charging, and instrument settings, segmented regions are defined as indicated damaged surface areas rather than direct chemical proof of corrosion products.

Despite the known risks of localized corrosion, a significant research gap remains in evaluating aircraft components exposed to real-world, coupled stressors. Existing literature

relies heavily on idealized material coupons, controlled salt-spray chambers, or static laboratory atmospheric exposures, which fail to replicate the synergistic effects of operational thermal gradients, mechanical fatigue, intermittent wet-dry transitions, and variable maintenance habits. Previous research by Hastuti et al. demonstrated that aluminum thermal arc spraying duration significantly influences coating adhesion quality [18], yet such studies do not capture in-service component degradation.

To address this limitation, the present study introduces a field-oriented approach by integrating multiscale quantitative SEM surface analysis at 300×, 500×, 800×, and 1000× magnifications (10 kV) of a service-degraded Cessna 172 seaplane brake caliper with detailed operational logs, maritime environmental data, and maintenance records from January 2022 to July 2026 (covering 3,891.9 flight hours, 3,442 landings, and 1,224 water landings). The objectives are to document the component-scale condition, identify dominant damage morphologies, quantify cross-scale surface parameters, and examine their relationship with maritime exposure and maintenance practices. Ultimately, this study provides a quantitative early-detection method to help evaluate component serviceability and optimize periodic maintenance schedules, providing a diagnostic foundation that future research can complement with SEM-EDX elemental verification and mass-loss or electrochemical corrosion-rate testing.

2. METHODS

Object, Period and Data Sources

The study examined the damaged surface of a dual-piston Cast Aluminum Alloy A356-T6 brake caliper removed from a Cessna 172 seaplane operated and maintained in a tropical maritime environment at the Indonesia Civil Pilot Academy (Akademi Penerbang Indonesia, API) in Banyuwangi, East Java, Indonesia. The investigated component is a Parker Cleveland brake caliper assembly (P/N 091-04400, system 30-75) with overall unit dimensions of 8.14 × 7.85 × 3.61 inches (206.8 × 199.4 × 91.7 mm) and a mass of 1.95 lbs (0.88 kg). Prior to microscopic examination, the initial surface condition of the service-degraded caliper was evaluated macroscopically alongside a reference brake caliper in visually good condition. In its initial as-removed state, the service-degraded caliper exhibited widespread flaking of its protective coating, dull gray metallic discoloration, reddish-brown and dark surface deposits inside and around the dual piston bores, and localized surface roughening across the housing face. The two macroscopic photographs were used solely to document and compare component-scale surface conditions and were not treated as matched experimental controls.

For microscopic evaluation, sampling was specifically localized on the flat caliper body surface located between the lower piston bore edge and the lower guide pin. This region was selected because its exposed flat geometry easily traps saline moisture and surface deposits while simultaneously experiencing mechanical vibrations and thermal stresses from the adjacent piston and guide pin during landing and braking. Alongside the physical specimen and four multiscale SEM images, the dataset comprised monthly operational records, environmental data, and inspection and maintenance histories from January 2022 to July 2026 (covering 3,891.9 flight hours, 3,442 total landings, and 1,224 water landings), with the 2026 values representing year-to-date records through July. Operational records included flight hours, total landings, and water landings. Environmental variables included salinity, relative humidity, temperature, and rainfall. Maintenance records included freshwater rinsing, missed rinses, rinse delay, lubrication, inspection, repainting, corrosion-preventive compound application, and inspection severity. All numerical records were compiled and cross-checked against the official aircraft logbooks, work orders, and institutional maintenance archives at Akademi Penerbang Indonesia Banyuwangi.

Specimen Preparation, SEM Acquisition, and Image Analysis

To prepare the specimen for SEM observation without altering its native in-service damage topography, the designated flat region between the lower piston bore edge and the lower guide pin was sectioned into a test coupon measuring approximately 10 × 10 × 5 mm using a cooled, low-speed precision saw to prevent thermal distortion. No mechanical grinding or polishing was performed on the target surface so that the original pits, deposit-attacked zones, exfoliation features, and microcracks remained intact. To remove residual hydraulic fluid, grease, and loosely adhered runway debris without disturbing intact corrosion features, the sectioned specimen was gently rinsed with distilled water and ultrasonically cleaned in analytical-grade ethanol for 10 minutes. Subsequently, the specimen was dried in a warm air stream, stored in a desiccator to prevent secondary atmospheric oxidation, and mounted onto an aluminum SEM holder stub using double-sided conductive carbon tape.

SEM images were acquired in secondary-electron mode at an accelerating voltage of 10 kV and a working distance of 10.2 to 10.3 mm. Images were recorded at 300× and 500× with 50 µm scale bars, at 800× with a 20 µm scale bar, and at 1000× with a 10 µm scale bar. Each scale bar was used to convert pixels to micrometers and to calculate the calibrated region of interest (ROI) within the SEM field of view. In ImageJ, images were converted to 8-bit format and processed through background correction (flattening), dark-feature enhancement, adaptive segmentation, noise removal, and object measurement. Based on the segmented 2D surface area profiles, object shapes, and fractal contours, specific damage morphologies were quantified. Pits were counted from segmented dark objects that satisfied predefined area, circularity, and local-intensity criteria. Equivalent pit diameter was calculated as $d = 2\sqrt{A/\pi}$. Pit density was obtained by dividing the pit count by the calibrated ROI area and was reported in pits/mm². Elongated dark features were skeletonized to assist in the detection of microcrack candidates, with each candidate visually verified. Fractal contour complexity was quantified as the fractal dimension using the box-counting method. Gray Ra, Gray Rq, and the surface roughness index describe only grayscale intensity variations in the 2D SEM images and are not equivalent to physical Ra or Rq values measured with a contact profilometer.

Exposure Indices And Statistical Analysis

The analytical workflow is summarized in Figure 1, whereas the definitions and interpretation limits of the principal parameters are presented in Table 1. The Chloride Exposure Index (CEI) was used to compare relative environmental exposure between observation periods. CEI is not a substitute for direct chloride-deposition measurements and is not an official ISO 9223 corrosivity category. Monthly CEI was calculated as:

$$\mathrm{CEI} = 100\left[0.45\left(\frac{S}{35}\right) + 0.30\left(\frac{RH}{100}\right) + 0.15\left(\frac{T}{30}\right) + 0.10\min\left(\frac{P}{300}, 1\right)\right] \qquad (1)$$

where S is salinity (PSU), RH is relative humidity (%), T is temperature (°C), and P is monthly rainfall (mm). A proposed Corrosion Susceptibility Index (CSI) combined CEI, cumulative water landings, flight hours, and service duration. As defined in Table 1, CSI was used to visualize cumulative exposure trends in support of component serviceability evaluation and periodic maintenance optimization, and must not be interpreted as a standalone airworthiness criterion. Data were summarized using the mean, standard deviation, coefficient of variation, range, and annual trend. Spearman rank correlation was used to explore relationships between the monthly inspection score and CEI, water landings, rinse compliance,

rinse delay, and delayed rinses. A value of $p < 0.05$ was treated as evidence of a statistical association in this exploratory analysis rather than proof of causation.

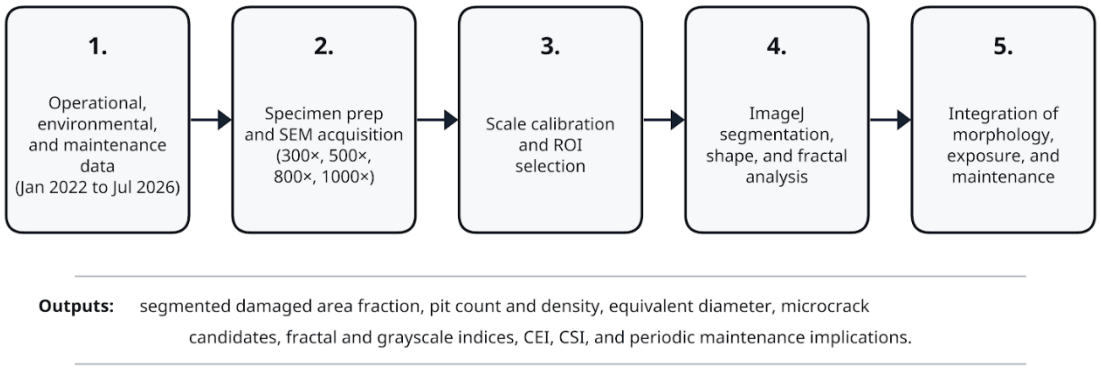


Figure 1. Research Workflow
Source: Research Data, 2026

Table 1. Definitions and Interpretation Limits of the Main Parameters

Parameter	Definition used in this study	Interpretation limit
Segmented damaged area fraction (%)	Segmented 2D damaged pixels divided by calibrated ROI area × 100	2D projected surface area only, not a 3D volume or direct chemical identification of corrosion products
Pit count and density (pits/mm²)	Objects filtered by area, circularity, and intensity, count divided by calibrated ROI area	Affected by SEM magnification and adaptive segmentation threshold settings
Equivalent pit diameter (µm)	Equivalent-circle diameter calculated from segmented 2D object area, $d = 2\sqrt{(A/\pi)}$	Represents 2D surface opening only, does not represent physical pit depth
Microcrack candidate	Elongated dark feature identified after skeletonization and visual verification	Surface trace indication, requires visual and cross-sectional confirmation
Fractal and grayscale indices	Box-counting fractal contour dimension and 2D SEM grayscale variations (Gray Ra, Gray Rq)	Describes 2D contour and brightness variation, not equivalent to contact profilometer Ra or Rq
CEI	Weighted monthly index of salinity, relative humidity, temperature, and rainfall	Proposed relative exposure index, not a direct deposition measurement or ISO 9223 category
CSI	Combined index of CEI, cumulative water landings, flight hours, and service duration	Supports periodic maintenance evaluation, not a standalone airworthiness criterion

Source: Research Data, 2026

3. RESULTS AND DISCUSSION

Operational Context And Maritime Environment

The operational records and maritime environmental conditions are summarized in Table 2, while their temporal trends are illustrated in Figure 2. During the observation period, the aircraft accumulated 3,891.9 flight hours, 3,442 landings, and 1,224 water landings. From 2022 to 2025, annual flight hours increased by 27.2%, while water landings increased by 50.7%. The proportion of water landings rose from 31.4% to 37.5% and reached 40.8% during January–July 2026. For the brake caliper, water-landing frequency represents maritime exposure more directly than flight hours alone. Each water operation provides an opportunity for saline moisture and salt deposits to remain on the wheel and brake assembly.

As also shown in Table 2 and Figure 2, mean annual salinity ranged from 33.02 to 33.53 PSU, relative humidity from 79.86% to 81.77%, and temperature from 27.73 to 28.13 °C. Annual CEI values were likewise relatively stable, ranging from 84.71 to 86.57, which corresponded to high to very high exposure under the internal study categories. Because annual

environmental conditions changed only slightly, the increase in inspection findings was likely influenced not only by weather but also by cumulative exposure, increasing water operations, coating condition, and the quality and timing of post-operation cleaning. This interpretation agrees with previous studies showing that chloride, humidity, temperature, rainfall, and time of wetness act together [4]–[8]. ISO 9223 likewise identifies airborne salinity and the combined effects of temperature and humidity as major factors. However, formal atmospheric-corrosivity classification requires chloride deposition or standard specimen mass loss data [2], [23].

Table 2. Summary of Aircraft Operation and Maritime Environmental Conditions

Year	Flight hours	Total landings	Water landings	Salinity (PSU)	RH (%)	CEI
2022	734.8	652	205	33.13	81.12	85.54
2023	812.5	718	239	33.53	79.86	84.71
2024	886.3	782	281	33.21	81.43	86.29
2025	934.7	824	309	33.37	80.63	85.28
2026 YTD	523.6	466	190	33.02	81.77	86.57
Total/mean	3,891.9	3,442	1,224	33.25	80.96	85.68

Source: Research Data, 2026

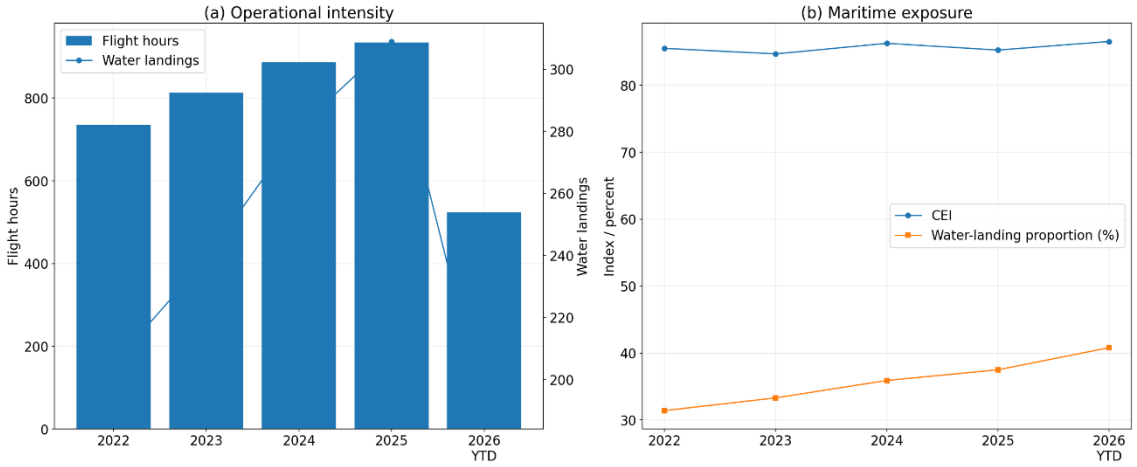


Figure 2. Trends in Aircraft Operation and Maritime Exposure
Source: Research Data, 2026

Macroscopic Comparison of Brake Caliper Condition

Macroscopic inspection was used to establish the component-scale context before SEM interpretation. The reference caliper in Figure 3(a) retained a relatively uniform metallic appearance, clearly defined machined surfaces, intact piston faces, and no obvious widespread deposits or coating breakdown. In contrast, the service-degraded caliper in Figure 3(b) exhibited extensive discoloration, brown and dark surface deposits, localized staining around the piston faces, abrasion marks, roughened regions, and loss of surface uniformity across the caliper body.

The visible deterioration was concentrated around recessed boundaries, piston-adjacent areas, and surface discontinuities where moisture and contaminants may be retained during repeated wet-dry cycles. This macroscopic evidence provides a direct component-level context for the subsequent SEM observation of pits, deposit-associated features, separated surface layers, and possible microcrack-like lines. Nevertheless, the photographic comparison is qualitative: color and texture alone cannot identify corrosion-product chemistry, quantify pit depth, or independently establish airworthiness. The designation of the degraded caliper as

unsuitable for continued service therefore reflects its maintenance disposition, whereas the present image analysis is used to characterize the observed surface damage.

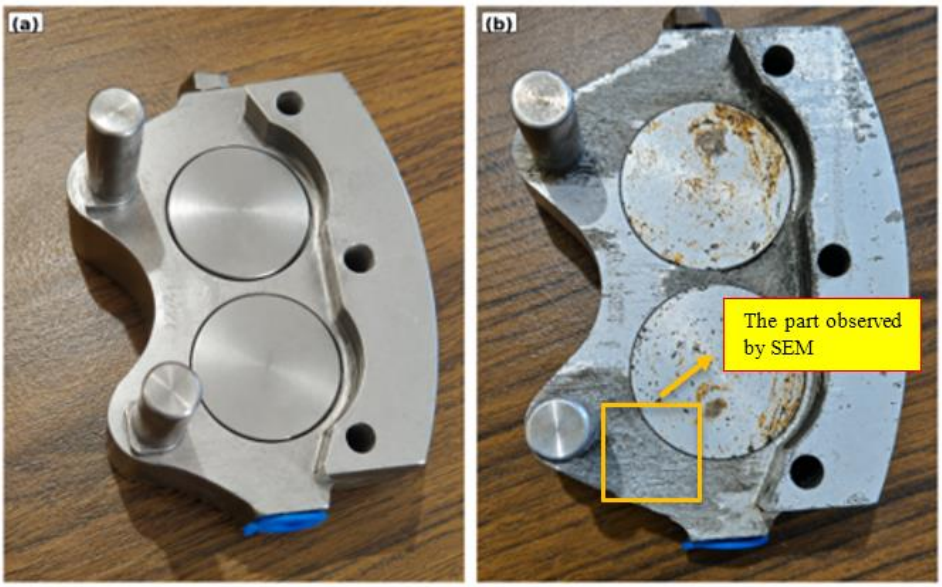


Figure 3. Macroscopic Condition of the A356-T6 Brake Caliper: (a) Visually Good Reference and (b) Service-Degraded Component Removed from Use
Source: Research Data, 2026

Surface Morphology at Different Magnifications

At 300× and 500×, the surface showed longitudinal grooves, circular and irregular cavities, clustered deposits, and raised or separated surface layers. At 800× and 1000×, smaller cavities became more distinct and nodular deposits appeared more abundant. Four main features were annotated in Figure 4: pitting, deposit-associated morphology, exfoliation-like layers, and microcrack candidates. The term exfoliation-like is used cautiously because definitive identification of exfoliation corrosion requires grain-orientation information, cross-sectional examination, and microstructural confirmation. Likewise, elongated dark lines cannot be classified as cracks without additional imaging or cross-sectional evidence.

The dispersed pits and the concentration of features around deposits are consistent with localized attack beneath a thin electrolyte layer. In A356-T6, localized corrosion may initiate at interfaces between the aluminum matrix and Fe-rich intermetallic particles, while eutectic silicon can act cathodically relative to the surrounding matrix [10], [11]. Chloride ions destabilize the passive film and may sustain pit growth in shielded or deposit-covered regions. With prolonged maritime exposure, pitting may develop into subsurface attack, cracking, or layer separation when the microstructure, casting porosity, residual stress, and coating condition are unfavorable [5], [6], [9], [13]. SEM morphology alone, however, cannot identify the elemental composition of deposits or corrosion products.

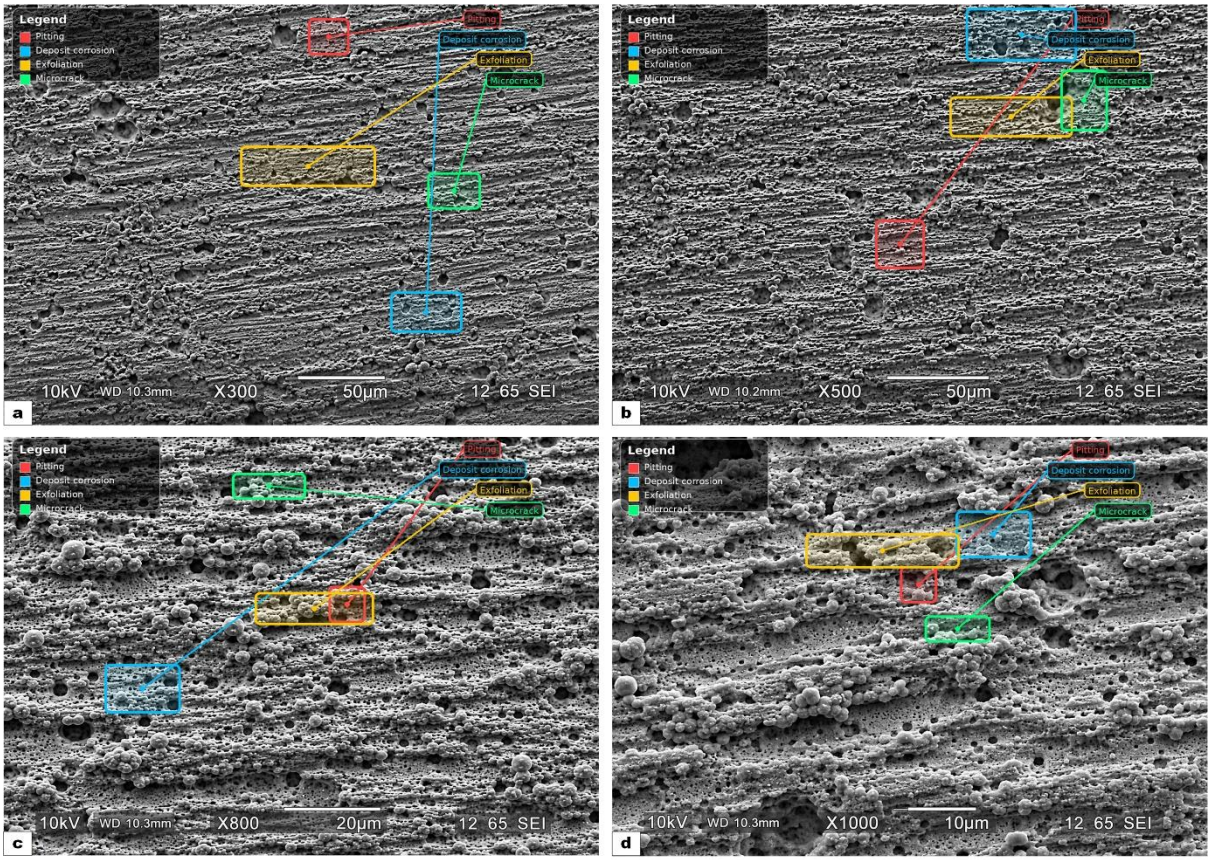


Figure 4. Morphological Features in SEM Images: (a) 300×, (b) 500×, (c) 800×, and (d) 1000×
Source: Research Data, 2026

Quantification of indicated area, pits, and surface complexity

The qualitative SEM observations presented in the previous section were further quantified using digital image analysis to evaluate the indicated damaged area, pit characteristics, and surface complexity across different SEM magnifications. The objective of this multiscale analysis was not to compare independent specimens but to determine whether the observed surface-damage pattern remained consistent when examined at different spatial resolutions.

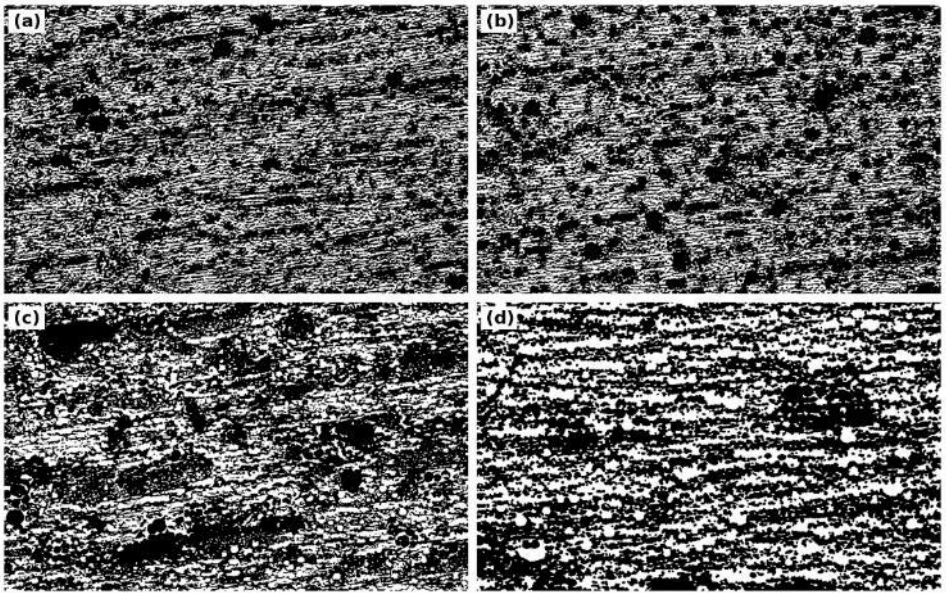


Figure 5. Binary Masks of Indicated Areas: (a) 300×, (b) 500×, (c) 800×, and (d) 1000×
Source: Research Data, 2026

Figure 5 presents the binary segmentation results used to identify the indicated damaged regions in each SEM image. Despite differences in field of view, the segmented regions occupied a comparable proportion of the observed surface at all four magnifications. The indicated damaged area ranged from 35.60% to 39.70%, with a cross-scale mean of 36.78 ± 1.95% and a coefficient of variation of 5.31%. The relatively small variation suggests that the damaged features were broadly distributed throughout the observed surface rather than being confined to a single localized region. The slightly higher value measured at 1000× is attributed to the smaller field of view, which captured an area containing a greater concentration of surface features. Accordingly, the four magnifications were not treated as independent statistical replicates but as complementary observations used to evaluate the consistency of the same damage pattern across multiple spatial scales.

Table 3. SEM Measurements and Digital Image Analysis Results

SEM	ROI (μm²)	Area (%)	Pit count	Pits/mm²	Mean d (μm)	D90 (μm)	Fractal dimension	SRI (%)
300×	73,178.95	35.95	2,938	40,148	1.076	1.513	1.921	24.62
500×	53,837.00	35.87	2,937	54,554	0.949	1.365	1.909	26.95
800×	19,147.11	35.60	2,556	133,493	0.691	1.157	1.880	20.63
1000×	2,400.49	39.70	296	123,308	0.410	0.623	1.863	27.10

Source: Research Data, 2026

Table 3 summarizes the quantitative parameters extracted from each SEM image. The detected pit count was 2,938 at 300×, 2,937 at 500×, 2,556 at 800×, and 296 at 1000×. Because the region of interest (ROI) became progressively smaller with increasing magnification, normalization by the observed area resulted in pit density increasing from 4.01×10^4 to a maximum of 1.33×10^5 pits/mm². This increase should not be interpreted as indicating more severe corrosion at higher magnification. Instead, the improved image resolution separates small pits that may appear merged when viewed at lower magnification. The same resolution effect is reflected by the decrease in the mean equivalent pit diameter from 1.08 μm to 0.41 μm, accompanied by reductions in D90 from 1.51 μm to 0.62 μm and in the maximum equivalent diameter from approximately 2.99 μm to 1.01 μm. These observations demonstrate that pit count and pit size are inherently dependent on image resolution and therefore should always be reported together with magnification, ROI area, pixel calibration, and segmentation criteria to ensure meaningful comparison between studies [3], [14].

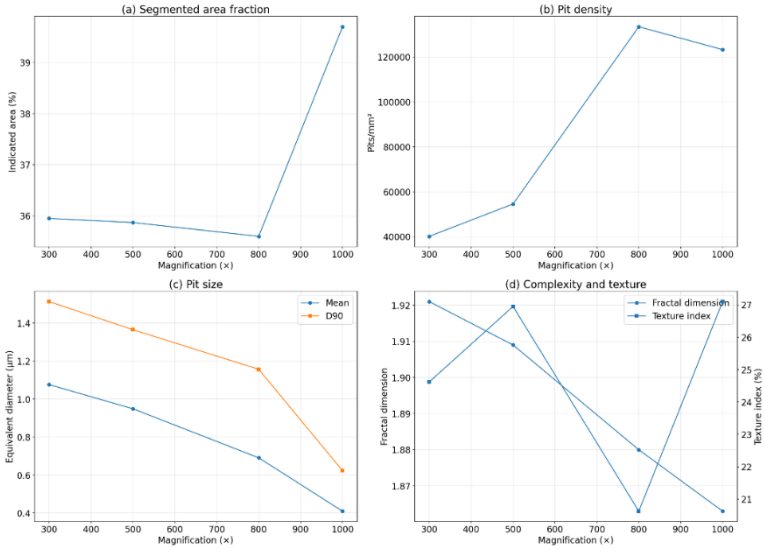


Figure 6. Quantitative Parameters at Different SEM Magnifications
Source: Research Data, 2026

The relationships among the principal quantitative parameters are illustrated in Figure 6. Although pit density increased with magnification, the indicated damaged area remained relatively stable, indicating that the principal effect of increasing resolution was the subdivision of previously unresolved small features rather than an increase in the overall damaged fraction. At the same time, the progressive reduction in equivalent pit diameter demonstrates that higher magnification improves the detection of fine-scale damage while preserving the overall spatial distribution identified at lower magnification. Consequently, lower magnifications are more appropriate for assessing the extent of surface degradation over a larger area, whereas higher magnifications provide greater sensitivity for characterizing individual pits and fine morphological details.

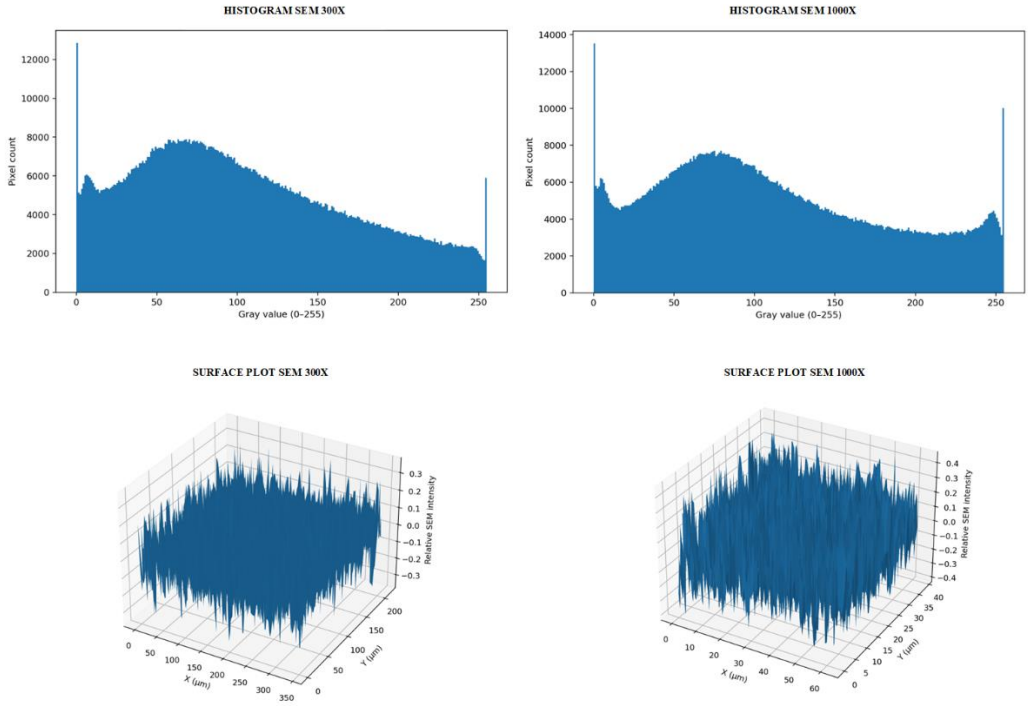


Figure 7. Histograms and Relative-Intensity Distributions at 300× and 1000×
Source: Research Data, 2026

Surface-boundary complexity was further evaluated using fractal analysis, which produced fractal dimensions ranging from 1.863 to 1.921 with excellent box-counting linearity (R^2 = 0.9976–0.9988). These values indicate that the segmented boundaries possessed irregular and complex geometries rather than smooth outlines. In addition, the grayscale-based surface roughness index (SRI) ranged from 20.63% to 27.10%, reflecting differences in image-intensity variation across the segmented regions. The grayscale histograms and relative-intensity profiles shown in Figure 7 exhibit sharper contrast transitions at 1000×, consistent with the improved resolution of smaller surface features. However, these grayscale-derived parameters represent only intensity variation in secondary-electron SEM images and should not be interpreted as physical roughness parameters such as Ra or Rq, nor should the vertical intensity axis be regarded as a direct measure of surface height. This distinction is important because a two-dimensional SEM image contains morphological information but does not directly provide three-dimensional topographic measurements.

As an extension of the present methodology, future image-based identification could incorporate SEM-EDX elemental mapping to distinguish corrosion products from non-corrosive deposits, integrate 3D surface profilometry for quantitative roughness validation, and apply machine-learning-based segmentation to improve the robustness and reproducibility of pit identification across different imaging conditions. Such developments would complement

the current multiscale image-analysis workflow while maintaining the standardized reporting framework recommended for quantitative corrosion-image analysis [3], [14].

Relationship between surface condition, maintenance, and inspection findings

The maintenance records and annual inspection summary are presented in Table 4, whereas the temporal relationships among rinse compliance, inspection findings, and the Corrosion Susceptibility Index (CSI) are illustrated in Figure 8. Maintenance records included 1,030 freshwater rinses, 50 lubrication activities, 40 inspections, and three repainting events. Although the number of rinses increased with water-landing activity, rinse compliance declined from 91.7% in 2022 to 75.3% in the 2026 year-to-date data. Mean rinse delay also increased from 1.46 to 3.33 h. Over the same period, the weighted finding score rose from 10 to 37, and CSI increased from 33.26 to 76.24. One severe finding was recorded in 2025 and two severe findings were recorded through July 2026. This pattern suggests that increasing exposure was not fully matched by timely rinsing and restoration of surface protection.

Analysis of 55 monthly observations, summarized in Figure 8, showed that inspection scores tended to be lower when rinse compliance was higher (Spearman $\rho = -0.302$; $p = 0.025$). In contrast, inspection scores increased with longer rinse delay ($\rho = 0.446$; $p < 0.001$) and with a greater number of rinses delayed by more than 2 h ($\rho = 0.391$; $p = 0.003$). The association with missed rinses was weaker ($\rho = 0.238$; $p = 0.080$). CEI was not significantly associated with inspection score ($\rho = 0.213$; $p = 0.119$), possibly because CEI remained within a consistently high and narrow range. These results do not establish rinse delay as the sole cause of damage. Coating condition, crevice geometry, contamination, brake temperature, casting defects, and repair quality may also contribute. Nevertheless, the observed pattern supports FAA guidance that cleaning, drying, inspection, and restoration of protective coatings should be performed consistently after exposure to a corrosive environment [1].

Table 4. Annual Maintenance and Inspection Findings

Year	Rinse compliance (%)	Rinse delay (h)	Inspections/100 water landings	Minor	Moderate	Severe	CSI
2022	91.71	1.46	3.90	7	1	0	33.26
2023	89.12	1.86	3.35	9	2	0	43.44
2024	83.99	2.34	3.20	11	3	0	55.55
2025	80.91	2.93	2.91	13	5	1	67.78
2026 YTD	75.26	3.33	3.16	10	5	2	76.24

Source: Research Data, 2026

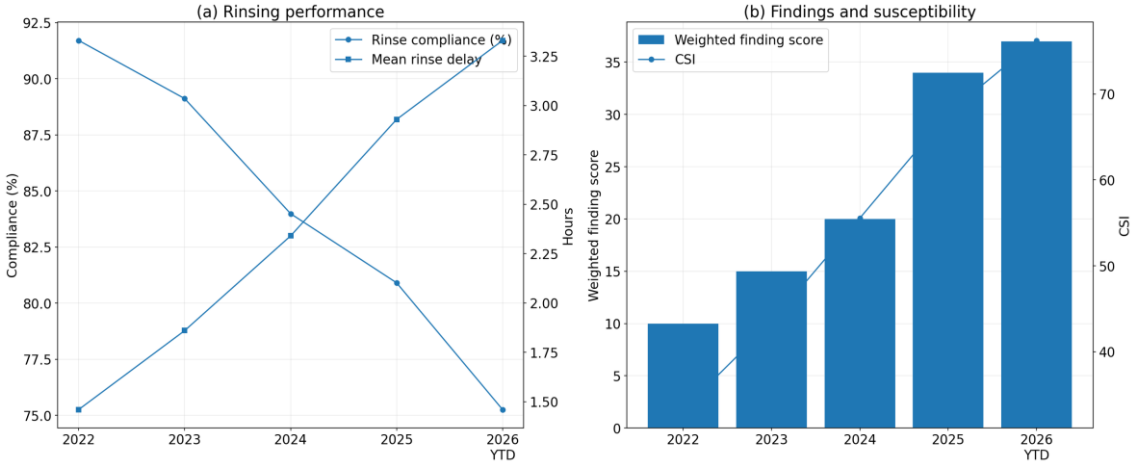


Figure 8. Rinse Compliance, Inspection Findings, and Susceptibility Index
Source: Research Data, 2026

Study contribution, validity, and limitations

The main strength of this study is the integration of macroscopic condition, SEM morphology from an actual service component, and nearly five years of operational and maintenance records. The photographic comparison documented the transition from a relatively uniform reference surface to a deposit-covered and visibly degraded service surface, while SEM resolved the associated micrometre-scale features. Unlike coupon tests that directly measure mass loss or penetration, the present approach provides image-based screening of surface condition. The relatively consistent indicated-area fraction, high pit density, nodular deposits, and separated surface layers show that the investigated surface was no longer homogeneous. Multiscale observation also clarified the effect of resolution: lower magnification was more suitable for evaluating the extent and distribution of damage, whereas higher magnification better resolved small pits and supported diameter measurement. Table 5 summarizes the principal similarities and differences between the present study and representative investigations reported in the literature.

Table 5. Comparison with Previous Studies

Study	Material/environment	Method	Relevant finding
Tian et al. [4]	2524-T3, several marine atmospheres	Exposure, SEM, and mechanical testing	Tropical conditions were most aggressive; defect depth was associated with degradation
Zhao et al. [5]	2024 alloy, South China Sea	12-month exposure and characterization	Early pitting developed into more extensive attack
Xiang et al. [6]	7075 alloy, marine atmosphere	Exposure and tensile testing	Pits and intergranular cracks promoted surface-layer separation
Peng et al. [7]	6061 alloy, wet-dry cycling	Simulated marine atmosphere	Longer wet periods increased corrosion damage
Present study	A356-T6 C172 seaplane brake caliper	Multiscale SEM, ImageJ, and operational records	Quantified service-component morphology and its relationship with maintenance

Source: Research Data, 2026

This study has several limitations. The damaged specimen was obtained from a single A356-T6 component and was examined at one time point. A visually good brake caliper was available only as a macroscopic reference; it was not sectioned or examined by SEM and was not a matched control with identical manufacturing, operating, exposure, and maintenance history. SEM-EDX, profilometry, cross-sectional microscopy, direct pit-depth measurement, mass-loss testing, and mechanical testing were not performed. Consequently, the present results cannot identify specific corrosion compounds, calculate corrosion rate, estimate remaining service life, or determine airworthiness. Dark segmented regions may also include topographic shadows or non-corrosive deposits. Future work should include repeated sampling at several component locations and independent image assessment by more than one analyst. SEM-EDX should be added to map Al, Si, Mg, O, and Cl and to distinguish corrosion products from environmental deposits. However, SEM-EDX does not measure corrosion rate by itself. Quantitative corrosion-rate assessment requires a time-dependent method, such as mass-loss immersion testing in accordance with ASTM G31 [29] or electrochemical measurement and calculation in accordance with ASTM G102 [30], preferably supported by profilometry and cross-sectional pit-depth measurements. Any decision to continue using the component must remain subject to the applicable maintenance manual and authorized engineering judgement.

4. CONCLUSION

Macroscopic comparison showed that the service-degraded caliper had lost the relatively uniform metallic appearance of the reference component and developed widespread discoloration, deposits, roughening, and localized surface deterioration. Multiscale SEM and

digital image analysis showed distributed surface damage on the Cast Aluminum Alloy A356-T6 brake caliper from a Cessna 172 seaplane. The indicated damaged area ranged from 35.60% to 39.70%, with pit densities of 4.01×10^{4}–1.33×10^{5} pits/mm² and mean equivalent pit diameters of 0.41–1.08 µm. The morphology was consistent with pitting, deposit-associated attack, exfoliation-like layers, and possible microcracks. SEM alone could not confirm elemental composition, corrosion-product chemistry, pit depth, or corrosion rate. During the study period, the aircraft accumulated 3,891.9 flight hours and 1,224 water landings under high to very high CEI conditions. Rinse compliance declined from 91.7% to 75.3%, while mean rinse delay increased from 1.46 to 3.33 h. The findings support immediate freshwater rinsing after water operations, documentation of delayed rinses, focused inspection of deposits and pits, and restoration of coatings or corrosion-preventive compounds in accordance with the maintenance manual. Future research should include SEM examination of a matched undamaged A356-T6 reference component, additional observation locations, SEM-EDX for elemental and corrosion-product identification, and mass-loss or electrochemical testing for quantitative corrosion-rate determination.

REFERENCES

[1] Federal Aviation Administration, Corrosion Control for Aircraft, Advisory Circular AC 43-4B. Washington, DC, USA: FAA, 2018.

[2] ISO 9223:2012, Corrosion of Metals and Alloys—Corrosivity of Atmospheres—Classification, Determination and Estimation. Geneva, Switzerland: International Organization for Standardization, 2012.

[3] ASTM G46-21, Standard Guide for Examination and Evaluation of Pitting Corrosion. West Conshohocken, PA, USA: ASTM International, 2021.

[4] H. Tian, Z. Cui, B. Zhang, W. Yang, Y. Yang, and H. Cui, "Atmospheric corrosion and mechanical property degradation of 2524-T3 aluminum alloy in marine environments," Corrosion Science, vol. 239, art. 112398, 2024, doi: 10.1016/j.corsci.2024.112398.

[5] J. Zhao, T. Zhao, Y. Zhang, Z. Zhang, Z. Chen, J. Wang, and M. Chen, "Corrosion behavior of the 2024 aluminum alloy in the atmospheric environment of the South China Sea Islands," Coatings, vol. 14, no. 3, art. 331, 2024, doi: 10.3390/coatings14030331.

[6] L. Xiang et al., "Impact of marine atmospheric corrosion on the microstructure and tensile properties of 7075 high-strength aluminum alloy," Materials, vol. 16, no. 6, art. 2396, 2023, doi: 10.3390/ma16062396.

[7] C. Peng, G. Cao, T. Gu, C. Wang, Z. Wang, and C. Sun, "The effect of dry/wet ratios on the corrosion process of the 6061 Al alloy in simulated Nansha marine atmosphere," Corrosion Science, vol. 210, art. 110840, 2023, doi: 10.1016/j.corsci.2022.110840.

[8] M. Gao, Z. Sun, W. Yan, Z. Tang, and Y. Zhang, "Influence of solid particles deposition on the initial atmospheric corrosion of 7B04 aluminum alloy," Materials Today Communications, vol. 31, art. 103562, 2022, doi: 10.1016/j.mtcomm.2022.103562.

[9] T. Cui et al., "Atmospheric corrosion behavior of typical aluminum alloys in low-temperature environment," Metals, vol. 15, no. 3, art. 277, 2025, doi: 10.3390/met15030277.

[10] C. Berlanga-Labari, M. V. Biezma-Moraleda, and P. J. Rivero, "Corrosion of cast aluminum alloys: A review," Metals, vol. 10, no. 10, art. 1384, 2020, doi: 10.3390/met10101384.

[11] R. Arrabal, B. Mingo, A. Pardo, M. Mohedano, E. Matykina, and I. Rodríguez, "Pitting corrosion of rheocast A356 aluminium alloy in 3.5 wt.% NaCl solution," Corrosion Science, vol. 73, pp. 342–355, 2013, doi: 10.1016/j.corsci.2013.04.023.

[12] H. Arima et al., "Seawater corrosion of the anodized A1050 aluminum plate for heat exchangers," Metals, vol. 15, no. 3, art. 300, 2025, doi: 10.3390/met15030300.

[13] J. Tao et al., "Corrosion behavior and mechanical performance of 7085 aluminum alloy in a humid and hot marine atmosphere," Materials, vol. 15, no. 21, art. 7503, 2022, doi: 10.3390/ma15217503.
[14] A. A. I. M. Ali et al., "Computer vision and image processing approaches for corrosion detection: A review," Journal of Marine Science and Engineering, vol. 11, no. 10, art. 1954, 2023, doi: 10.3390/jmse11101954.
[15] C. A. Schneider, W. S. Rasband, and K. W. Eliceiri, "NIH Image to ImageJ: 25 years of image analysis," Nature Methods, vol. 9, no. 7, pp. 671–675, 2012, doi: 10.1038/nmeth.2089.
[16] C. T. Rueden et al., "ImageJ2: ImageJ for the next generation of scientific image data," BMC Bioinformatics, vol. 18, art. 529, 2017, doi: 10.1186/s12859-017-1934-z.
[17] A. B. Schroeder et al., "The ImageJ ecosystem: Open-source software for image visualization, processing, and analysis," Protein Science, vol. 30, no. 1, pp. 234–249, 2021, doi: 10.1002/pro.3993.
[18] S. Hastuti, I. N. Hadi, C. Pramono, B. Pandupradityo, and Larasanto, "Effect of aluminum thermal arc spray duration on coating adhesion," V-MAC, vol. 9, no. 2, pp. 1–7, 2024, doi: 10.36526/v-mac.v9i2.3378. [In Indonesian].
[19] B. Leng et al., "A critical review of anti-corrosion chemical surface treatment methods for aluminum alloys," Crystals, vol. 14, no. 1, art. 101, 2024, doi: 10.3390/cryst14010101.
[20] G. S. Frankel, "Pitting corrosion of metals: A review of the critical factors," Journal of The Electrochemical Society, vol. 145, no. 6, pp. 2186–2198, 1998, doi: 10.1149/1.1838615.
[21] Z. Szklarska-Smialowska, "Pitting corrosion of aluminum," Corrosion Science, vol. 41, no. 9, pp. 1743–1767, 1999, doi: 10.1016/S0010-938X(99)00012-8.
[22] N. Birbilis and R. G. Buchheit, "Electrochemical characteristics of intermetallic phases in aluminum alloys: An experimental survey and discussion," Journal of The Electrochemical Society, vol. 152, no. 4, pp. B140–B151, 2005, doi: 10.1149/1.1869984.
[23] J. J. Santana et al., "Shortcomings of International Standard ISO 9223 for the classification, determination, and estimation of atmosphere corrosivity in subtropical archipelagic conditions," Metals, vol. 9, no. 10, art. 1105, 2019, doi: 10.3390/met9101105.
[24] M. Montoya et al., "The AA7075–CS1018 galvanic couple under evaporating saline droplets," Corrosion and Materials Degradation, vol. 5, no. 1, art. 5, 2024, doi: 10.3390/cmd5010005.
[25] M. Kim et al., "Effect of microstructure on corrosion behavior of cold-sprayed AA5083 compared with wrought AA5083," Corrosion and Materials Degradation, vol. 5, no. 1, art. 2, 2024, doi: 10.3390/cmd5010002.
[26] S. Suhartini et al., "Sustainable corrosion protection: Chitosan/reduced graphene oxide nanocomposite coating derived from palm oil empty fruit bunches on low carbon steel," Case Studies in Chemical and Environmental Engineering, vol. 11, art. 101116, 2025, doi: 10.1016/j.cscee.2025.101116.
[27] G. M. Kamath, P. D. Mangalgiri, and A. Shet, "A quantitative assessment of the impact of corrosion on fatigue life of aircraft components," Engineering Failure Analysis, vol. 135, art. 105973, 2022, doi: 10.1016/j.engfailanal.2021.105973.
[28] H. Song, C. Liu, H. Zhang, J. Du, X. Yang, and S. B. Leen, "In-situ SEM study of fatigue micro-crack initiation and propagation behavior in pre-corroded AA7075-T7651," International Journal of Fatigue, vol. 139, art. 105655, 2020, doi: 10.1016/j.ijfatigue.2020.105655.
[29] ASTM G31-21(2025), Standard Guide for Laboratory Immersion Corrosion Testing of Metals. West Conshohocken, PA, USA: ASTM International, 2025.

[30] ASTM G102-23, Standard Practice for Calculation of Corrosion Rates and Related Information from Electrochemical Measurements. West Conshohocken, PA, USA: ASTM International, 2023.